

The Influence of Swell on the Atmospheric Boundary Layer under Nonneutral Conditions

ZHONGSHUI ZOU,^{a,b,c} DONGLIANG ZHAO,^{b,c} JUN A. ZHANG,^{d,e} SHUIQING LI,^{f,c} YINHE CHENG,^a
HAIBIN LV,^a AND XIN MA^{b,c}

^a *School of Geomatics and Marine Information, Huaihai Institute of Technology, Lianyungang, China*

^b *Physical Oceanography Laboratory, Ocean University of China, Qingdao, China*

^c *Qingdao National Laboratory for Marine Science and Technology, Qingdao, China*

^d *Cooperative Institute for Marine and Atmospheric Studies, University of Miami, Miami, Florida*

^e *Hurricane Research Division, NOAA/AOML, Miami, Florida*

^f *Key Laboratory of Ocean Circulation and Waves, Institute of Oceanology, Chinese Academy of Sciences, Qingdao, China*

(Manuscript received 22 September 2017, in final form 26 February 2018)

ABSTRACT

The anomalous phenomena induced by the prevailing swell at low wind speeds prevent a complete understanding of air–sea interaction processes. Many studies have considered this complex problem, but most have focused on near-neutral conditions. In this study, the influence of the swell on the atmospheric boundary under nonneutral conditions was addressed by extending the turbulent closure models of Makin and Kudryavtsev and the Monin–Obukhov similarity theory (MOST; Monin and Yaglom) to the existence of swell and nonneutral conditions. It was shown that wind profiles derived from these models were consistent with each other and both departed from the traditional MOST. At low wind speeds, a supergeostrophic jet appeared on the upper edge of the wave boundary layer, which was also reported in earlier studies. Under nonneutral conditions, the influence of buoyancy was significant. The slope of the wind profile increased under stable conditions and became smoother under unstable conditions. Considering the effects of buoyancy and swell, the wind stress derived from the model agreed quantitatively with the observations.

1. Introduction

Unlike the rigid land surface, the ocean surface fluctuates at various scales, ranging from millimeters to hundreds of kilometers. Ocean waves, which are generated by surface wind, play a crucial role in the dynamical processes that occur in the lower atmosphere and upper ocean. During the last decade, many efforts have been made to parameterize the momentum, heat, and vapor fluxes over oceans. The most well known of these is the state-of-the-art Coupled Ocean–Atmosphere Response Experiment (COARE) algorithm (Fairall et al. 2003).

Even so, some anomalous phenomena occur at low wind speeds, when the prevailing swell is difficult to clarify. The swell is typically characterized as long waves that are generated by storms and are transported more rapidly than the local wind. In general, ocean swells do not absorb energy from the local wind, but they do excite

the upward momentum flux, which leads to an anomalous interaction between the ocean and atmospheric boundary layer (ABL). For example, Harris (1966) first found that a weak wave-driven wind is always present above the wave in a wave tank. Donelan et al. (1997) showed that the presence of a counter- and cross swell can generate a larger drag coefficient than pure wind sea conditions. In this situation, the momentum flux estimated by the eddy correlation method is not consistent with that estimated by the inertial dissipation method. Smedman et al. (1999) indicated that the swell can transfer momentum from waves to the atmosphere by pressure, leading to a small net momentum flux. Drennan et al. (1999) reported that the momentum spectra and cospectra in the presence of swell deviate from the universal spectra shape, and the Monin–Obukhov similarity theory (MOST; Monin and Yaglom 1971) is invalid. The Tropical Ocean and Global Atmosphere (TOGA) COARE datasets also show that cospectral energy decreases monotonically with wind speed, whereas there is an inverse relationship

Corresponding author: Dongliang Zhao, dlzhao@ouc.edu.cn

DOI: 10.1175/JPO-D-17-0195.1

© 2018 American Meteorological Society. For information regarding reuse of this content and general copyright information, consult the AMS Copyright Policy (www.ametsoc.org/PUBSReuseLicenses).

for wind speed below about 1.5 m s^{-1} (Grachev and Fairall 2001). Other studies have identified the presence of low-level jets (Miller et al. 1999) and a negative gradient mean profile (Rutgersson et al. 2001), which are related to the swell.

To explicitly illustrate such phenomenon, many models have been developed in the last decade, including the direct numerical simulation (DNS; Sullivan et al. 2000; Kihara et al. 2007), large-eddy simulation (LES; Sullivan et al. 2008; Nilsson et al. 2012; Sullivan et al. 2014; Jiang et al. 2016), and one-dimensional model (Hanley and Belcher 2008; Semedo et al. 2009; Song et al. 2015). All of these models can qualitatively and quantitatively capture the interaction between swell and atmosphere, including the wave-driven jets, negative gradient mean profile, and upward surface stress. Although the wave boundary layer is only a few times higher than the characteristic wave height, these results suggest that the impact of swell can penetrate throughout the whole boundary layer and lead to the invalidation of MOST. By dividing the momentum cospectra into low-, middle-, and high-frequency bands, Rieder and Smith (1998) and Högström et al. (2015) found that swell-induced stress is related to the significant wave height and dominates the cospectra frequency.

The prevailing swell in the ocean poses a significant challenge to the understanding of air–sea interaction processes. Although the studies mentioned above have provided new insights into this complex problem, most have focused on near-neutral conditions. To the best of our knowledge, only Nilsson et al. (2012) and Sullivan et al. (2014) have investigated the unstable boundary layer in the presence of swell. At low wind speeds, the buoyancy effect is another key factor that influences the ABL. Therefore, the focus of this study was to clarify the differences between the impact of swell on nonneutral and neutral ABLs. To address this issue, a constant flux model based on two turbulent closure schemes was applied. One scheme was from Makin and Kudryavtsev (1999, hereinafter MK99), and the other was from MOST. The MK99 method was originally used to study the effect of wind waves on the drag coefficient under neutral conditions. Here, we extended this model to swell and nonneutral conditions (MKS). The MOST method has been widely used to calculate momentum based on the Charnock relationship (Charnock 1995), whereas in this study the wave-spectrum-based method was applied. To distinguish this method from the traditional MOST, it will be referred as MOS hereinafter.

This paper is organized as follows. The constant flux model with two turbulent closure schemes is described in section 2. The behavior of the model is presented in

section 3. In section 4, the results are compared with measurements, and conclusions are provided in section 5.

2. Constant flux model

In this study, the constant flux model was used to analyze the influence of swell on ABLs under non-neutral conditions. The model assumes that the total stress is independent of height in the lower part of the ABL:

$$\frac{\partial \tau}{\partial z} = 0, \quad (1)$$

where z is the vertical coordinate, which is positive upward; and τ is the wind stress defined as $-\overline{w'u'}$, where w' and u' are the fluctuations of vertical and horizontal wind velocity and the overbar indicates that it is a time-averaged process. The air density ρ_a in the definition of wind stress is omitted for simplicity. The wind stress is supported by the sum of the turbulent stress τ_t , viscous stress τ_{vis} , and wave-induced stress τ_w :

$$\tau = \tau_t + \tau_{\text{vis}} + \tau_w = u_*^2, \quad (2)$$

where u_* is friction velocity. To estimate the total wind stress, the above three stresses should first be specified. At low wind speeds, the water surface is aerodynamically smooth and always exists as a viscous sublayer. At the sea surface $z = 0$, the total stress is controlled by the viscous stress. However, the viscous stress can be neglected farther from the water surface, and the wind stress can be expressed as follows:

$$\tau = \tau_t(z) + \tau_w(z). \quad (3)$$

To avoid the explicit description of the stress within the viscous sublayer, Makin et al. (1995) and Makin and Kudryavtsev (1999) provided a viscous roughness scale at the top of the viscous sublayer:

$$z_0^v = 0.1 \frac{\nu}{u_{*0}^l}, \quad (4)$$

where ν is the kinematic viscosity of air, and u_{*0}^l is the friction velocity at the top of the viscous sublayer:

$$(u_{*0}^l)^2 = \tau - \tau_w(z_0^v). \quad (5)$$

The turbulent stress is related to the gradient of velocity via eddy viscosity based on the first-order closure method:

$$\tau_t = K_m \frac{\partial U}{\partial z}, \quad (6)$$

where U is wind speed and K_m is eddy viscosity, which can be a constant or a function of height, wind shear, or stability. Many previous studies, such as those of [Makin et al. \(1995\)](#), [Hanley and Belcher \(2008\)](#), and [García-Nava et al. \(2012\)](#), expressed the eddy viscosity as follows:

$$K_m = l^2 \left| \frac{\partial U}{\partial z} \right|, \tag{7}$$

where $l = \kappa z$ is the mixing length and κ is the von Kármán constant. [Makin and Kudryavtsev \(1999\)](#) have shown that this can lead to an underestimation of the eddy viscosity and an overestimation of the growth rate parameter. By analyzing the turbulent kinetic energy (TKE) function, they obtained the eddy viscosity under neutral conditions:

$$K_m = lu_* \left[1 - \frac{\tau_w(z)}{u_*^2} \right]^{1/4}. \tag{8}$$

At low wind speeds, buoyancy production plays an important role in the turbulence in the ABL, and the TKE function becomes

$$P + B = \varepsilon, \tag{9}$$

where

$$P = [\tau_t(z) + \tau_w(z)] \frac{\partial U}{\partial z} = u_*^2 \frac{\partial U}{\partial z} \tag{10}$$

represents the turbulence generated by shear, and the buoyancy production is given by

$$B = \frac{g}{\theta} \overline{w'\theta'}, \tag{11}$$

where g is the acceleration of gravity, θ is the potential temperature, and $\overline{w'\theta'}$ is the heat flux between the atmosphere and ocean. The term on the right side of Eq. (9) represents the viscous dissipation of TKE ([Makin and Kudryavtsev 1999](#)):

$$\varepsilon = K_m^3 l^{-4}. \tag{12}$$

Combining Eqs. (3) and (6) with Eq. (9), the eddy viscosity under nonneutral conditions can be expressed as

$$K_m^4 l^{-4} + K_m \frac{u_*^3}{\kappa z} \frac{z}{L} = \tau |\tau - \tau_w(z)|, \tag{13}$$

where $L = -u_*^3 \theta / g \kappa \overline{w'\theta'}$ is the Obukhov length scale. Under neutral conditions $z/L = 0$, Eq. (13) reduces to Eq. (8).

The wave-induced stress represents a loss of momentum from the airflow. The surface value of the wave-induced stress is given by integration of the wave-induced stress going into each wave component:

$$\tau_w(0) = \int_0^\infty \rho_w \omega \beta \Phi(\omega) d\omega, \tag{14}$$

where ω is the angular frequency, $\Phi(\omega)$ is the frequency spectrum, and β is the wave growth/decay rate. The wave-induced stress decays with height z according to approximately $\exp(-2kz)$ ([Semedo et al. 2009](#)); thus, the vertical distribution of wave-induced stress is given by

$$\tau_w(z) = \tau_w(0) e^{-2kz}. \tag{15}$$

Equation (15) shows that the wave-induced stress controls a significant part of the total stress near the sea surface, where turbulent stress must be reduced owing to the conservation of momentum flux. Outside of the wave boundary layer, the stress is completely supported by turbulent flux. With the definition of wave-induced stress as well as Eqs. (3), (6), and (13), the wind profile above the wave field can be written as follows:

$$U(z) = \int_{z_0^p}^z [\tau - \tau_w(z)] K_m^{-1} dz \tag{16}$$

For comparison, we also considered the traditional mixing length model $K_m = \kappa u_* z$. According to MOST ([Monin and Yaglom 1971](#)), the eddy viscosity under nonneutral conditions can be given by

$$K_m = \kappa u_* z / \phi(z/L), \tag{17}$$

where ϕ is dimensionless shear ([Högström 1988](#)). By substituting Eq. (17) into (16), the following can be obtained:

$$U(z) = \frac{\tau}{\kappa u_*} \left[\ln \left(\frac{z}{z_0^p} \right) - \Psi \left(\frac{z}{L} \right) \right] - \frac{\tau_w(0)}{\kappa u_*} \int_{z_0^p}^z \frac{\phi e^{-2kz}}{z} dz, \tag{18}$$

where Ψ is the integral of dimensionless shear from the viscous roughness scale to height z . Under neutral conditions $\Psi = 0$ and $\phi = 1$, Eq. (18) is equal to Eq. (25) in [Semedo et al. \(2009\)](#). In the absence of the wave field, the element roughness at the sea surface is controlled by the viscosity, and the second term on the right-hand side of Eq. (18) vanishes. Thus, the wind profile reduces to the traditional well-known MOST. The wave-induced stress introduces a new term that modifies the MOST. For wind waves, the new term is positive and decreases

with height, which makes the wind profile steeper. This means that the more waves there are on the sea surface, the rougher the sea surface. However, as shown below, for swells, the wave-induced stress is negative and makes the wind profile smoother. As the swells dominate the wave field, the sign of the wind-induced stress reverses and a jet is induced.

3. Behavior of the model

The behavior of the model was estimated. For clarity, the results of the eddy viscosities computed by Eqs. (8) and (13) are referred to as MK99 and MKS, respectively. The wind profile calculated by Eq. (18) is referred to as MOS in order to distinguish it from the traditional MOST.

Before the models were evaluated, the wave growth/decay rate β and the wave spectrum were specified. The wave growth/decay rate describes the rate of growth or decay of a wave spectrum. In a study of sea surface drag estimated from the wind speed and the sea state, Makin et al. (1995) gave a detailed review of the wave growth/decay rate. According to Belcher and Hunt (1993), it can be written as follows:

$$\beta = \frac{dE/dt}{E} = c_\beta \omega \frac{\rho_a}{\rho_w} \left(\frac{u_{*0}^l}{c} \right)^2, \quad (19)$$

where E is wave energy, c_β is the wave growth/decay rate coefficient, and ρ_a and ρ_w are the air and water density, respectively. By combining laboratory and field experiment data, Plant (1982) showed that c_β has a value of about 32 ± 16 for a wave age $cu_* < 20$. However, for greater wave ages or faster waves, the value is negative and strongly dependent on the turbulent closure model (Belcher and Hunt 1993; Cohen and Belcher 1999). To avoid the complication of the turbulent closure model, we selected a value of $c_\beta = -30$ for $cu_* \geq 20$ to qualitatively describe the behavior of the model (Hanley and Belcher 2008).

Usually, the wave spectrum can be separated into peak regions, an equilibrium range, and a dissipation range, with the frequency increasing successively. Several studies have shown that the equilibrium range plays a significant role in the wind-induced stress. However, the upper limiting frequency of most observations or wave models is limited to a peak region and is far from the equilibrium range. To compensate for the lost part of the spectrum, many studies have used an empirical whole-range wave spectrum: for example, Kudryavtsev and Makin (2001), Makin and Kudryavtsev (2002), and Mueller and Veron (2009) adopted the spectrum introduced by Elfouhaily et al. (1997), whereas

Makin et al. (1995) and Hanley and Belcher (2008) used a spectrum based on Donelan et al. (1985). Another possible method is to add a high-frequency tail to the observed or modeled spectrum (e.g., García-Nava et al. 2012; Moon et al. 2004; Reichl et al. 2014).

It was noted that the wave-induced stress was dominated by the ω^{-4} region of the spectrum. This means that waves with steep slopes were strongly coupled to the wind, but waves in the vicinity of the spectral peak with lower slopes were weakly coupled to the wind. We assumed a region existed in which wind waves were generated by local light winds and swell that were generated by distant storms propagated into the region. This situation is conducive to wave-driven wind. In this study, following Hanley and Belcher (2008), the frequency spectrum of the wind waves was calculated using the formula suggested by Donelan et al. (1985):

$$\Phi_0(\omega) = \alpha g^2 \omega^{-4} \omega_p^{-1} \exp[-(\omega_p/\omega)^4] \Gamma, \quad (20)$$

where

$$\Gamma = \exp[-(\omega - \omega_p)^2 / 2\sigma^2 \omega_p^2], \quad (21)$$

with $\alpha = 0.006(U_{10}/c_p)^{0.55}$, $\sigma = 0.08[1 + 4(U_{10}/c_p)^3]$, $\Gamma = 1.7 + 6.0 \log(U_{10}/c_p)$, ω_p is the frequency at the peak of the spectrum, U_{10} is the wind speed at a height of 10 m, and c_p is the phase speed at the peak of the spectrum.

We assumed that the wind waves generated by high winds propagated at their group speed and lost their energy. After propagating thousands of kilometers into a light wind region, the short waves were mostly damped, with the long waves remaining. The resulting spectrum was then typical of swell with long waves, but with very little energy in the short waves. The wind waves were also generated by the local light winds; thus, the spectrum in this region was the sum of the spectrum of wind waves generated by local light winds and the spectrum of swells generated by distant high winds. Both could be expressed by Φ_0 , but the latter was multiplied by a damping factor due to the propagation. Therefore, the wave spectrum in a region with light winds can be written as follows:

$$\Phi(\omega) = \Phi_{0l}(\omega) + \Phi_{0h}(\omega) \exp\left[\left(\frac{\omega}{\omega_0}\right)^3\right], \quad (22)$$

where Φ_{0l} and Φ_{0h} are the spectra of wind waves generated by the local light winds and distant high winds, respectively. Both are calculated from Eq. (20). Here, ω_0 is the damping parameter, and $\omega_0^3 = -0.01$ was used in this study (Hanley and Belcher 2008).

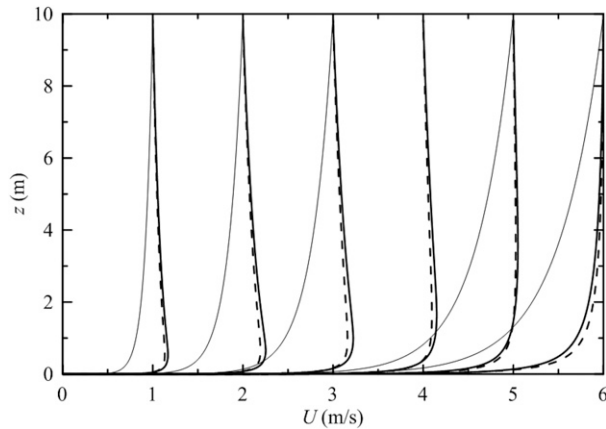


FIG. 1. The influence of swell on the wind profile under neutral conditions. Here, a 10-m-height wind speed ranging from 1 to 6 m s^{-1} was selected. The thick, solid lines use a turbulent model closure by MKS and the dashed lines use MOS. It should be noted that under neutral conditions, MKS reduced to MK99. For comparison, wind profiles derived from the traditional MOST based on COARE 3.5 (thin, solid lines) are included.

After the definition of growth rate and the wave spectrum, the solution of Eq. (16) or (18) could be calculated iteratively. Figure 1 shows the wind profiles calculated by two turbulent closure models under neutral conditions. Here, the high wind speed was 15 m s^{-1} , and the low wind speeds ranged from 1 to 6 m s^{-1} at a height of 10 m, with a wave age $c_p/U_{10} = 1.2$ selected to specify Φ_{0h} and Φ_{0l} . Additionally, wind profiles derived from MOST and based on COARE 3.5 (Edson et al. 2013) were plotted for comparison. The figure shows that the influence of swell on the wind profile was remarkable. Without swell, the wind profile decreased exponentially with height. Under swell conditions, the wind profiles departed from the traditional MOST and the slopes of the wind profiles decreased because the viscous roughness was reduced [Eqs. (4) and (5)], which was ascribed to the negative stress produced by the swell. When the local wind speed decreased further, a supergeostrophic jet appeared on the upper edge of the wave boundary layer. This feature has also been reported in previous studies, such as Hanley and Belcher (2008), Sullivan et al. (2008), and Semedo et al. (2009).

A comparison between the two models showed that they were consistent with each other. However, the MKS jet strength (maximum wind) and the height of the maximum wind were slightly larger than in the MOS model. It should be noted that these features are not in conflict with previous studies, for example, the height of the jet in Semedo et al. (2009) is 3 m, because they depend on the swell spectrum and the wave growth rate β .

The total wind stress, turbulent stress, and wave-induced stress at local wind speeds of 6 and 2 m s^{-1} are shown in

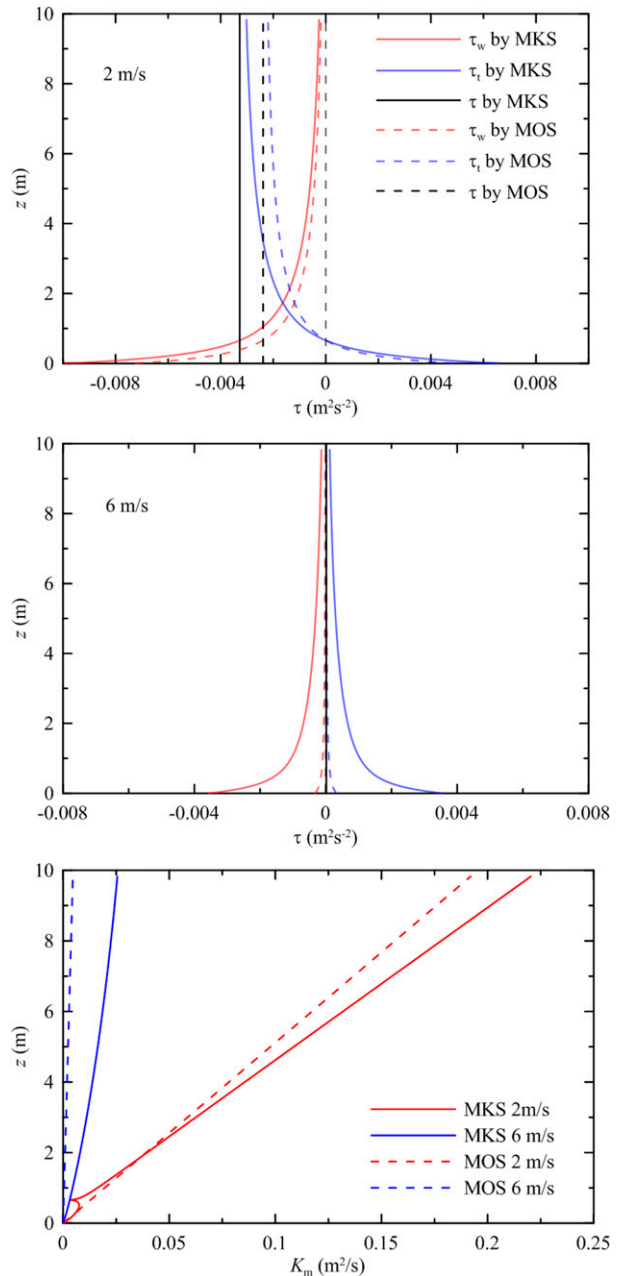


FIG. 2. The total wind stress, turbulent stress, and wave-induced stress profiles and the eddy viscosity profile at wind speeds of (top) 2 and (bottom) 6 m s^{-1} .

Fig. 2, which provides a detailed view of the model. It can be seen that the wave-induced stress τ_w decays exponentially with height. At $U_{10} = 6 \text{ m s}^{-1}$, the stress generated by shear is positive, but at 2 m s^{-1} it is positive only within the wave boundary layer and changes sign outside of this layer, which is consistent with the wind profile shown in Fig. 1.

The total stress is the sum of wave-induced stress and turbulent stress. At $U_{10} = 6 \text{ m s}^{-1}$, the total stress is

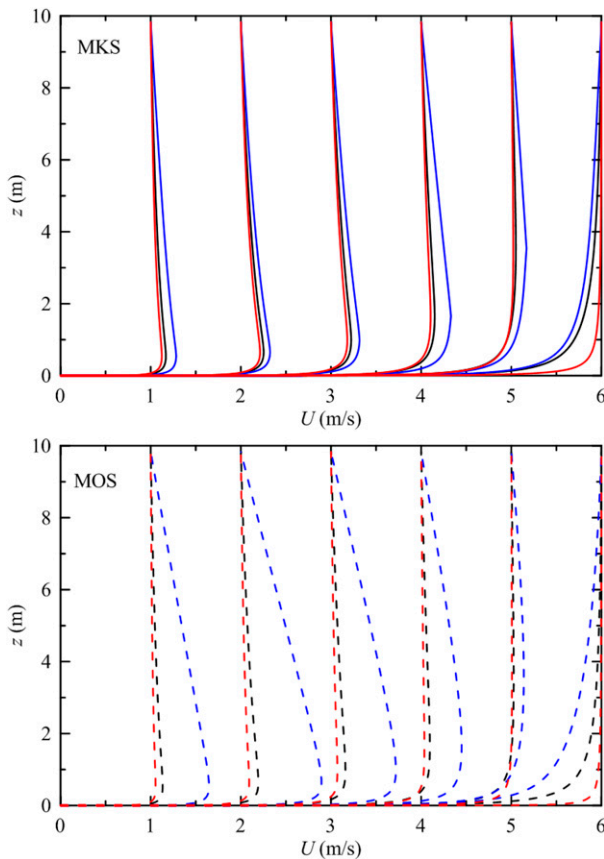


FIG. 3. The wind profile under nonneutral conditions from (top) MKS and (bottom) MOS. The black lines show the wind profile under neutral conditions, and the red and blue lines show the wind profiles under unstable and stable conditions, respectively.

positive because the turbulent stress contributed most to the total stress. With a decrease in wind speed, the effect of swell on the stress increased, leading to a negative value. A comparison between the two methods showed that the amplitude of total stress derived by MKS was slightly larger than that derived by MOS. This was a common feature for the other wind speeds.

A significant difference between the two models was found in the jet, where the turbulent stress became zero. At this time, the stress was completely controlled by wave-induced stress that resulted in the eddy viscosity becoming zero with the MKS. Below the jet, the eddy viscosity first increased with depth and then decreased. Above the jet, the eddy viscosity increased with height, which was similar to MOS.

The influence of buoyancy on the model was investigated by considering the temperature difference $\Delta\theta$ ($\Delta\theta = \theta_{10} - \theta_0$) between 10 m and the sea surface. Here, $\Delta\theta = \pm 0.5^\circ\text{C}$, with $\theta = 20^\circ\text{C}$ used to calculate the heat flux $\overline{w'\theta'} = -C_H U \Delta\theta$, where C_H is the heat transfer coefficient. It was shown experimentally that

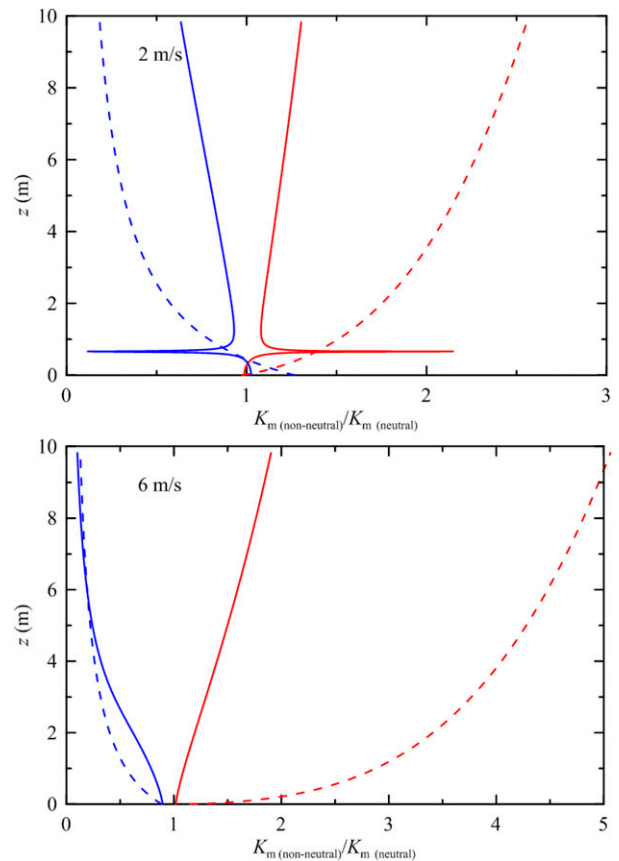


FIG. 4. The ratio of eddy viscosity between nonneutral and neutral conditions at wind speeds of (top) 2 and (bottom) 6 m s^{-1} . The solid lines represent the eddy viscosity derived by MKS, and the dashed line is derived by MOS. The red and blue lines represent unstable and stable conditions, respectively.

$\theta \pm 10^\circ\text{C}$ did not substantially change the final result. It has not been previously reported that the swell could influence the heat transfer coefficient, and we used a value of 1.1×10^{-3} given by Large and Pond (1982) to calculate the heat flux.

According to turbulence theory (Kundu et al. 2012), a stable situation ($\Delta\theta > 0$) can suppress the turbulence that leads to an increased slope of the wind profile, whereas an unstable situation ($\Delta\theta < 0$) can enhance the turbulence and make the slope of the wind profile smoother. The results shown in Fig. 3 are consistent with this theory. Figure 3 also shows that the influence of buoyancy on the model was remarkable. The strength of the jet was enhanced in stable conditions and became weaker in unstable conditions. A more surprising phenomenon was the wind profile at 5 m s^{-1} . Under stable conditions, both MKS and MOS generated a jet, whereas this was not found under neutral and unstable conditions.

Figure 4 gives the ratio of eddy viscosity between nonneutral and neutral conditions. It can be seen that

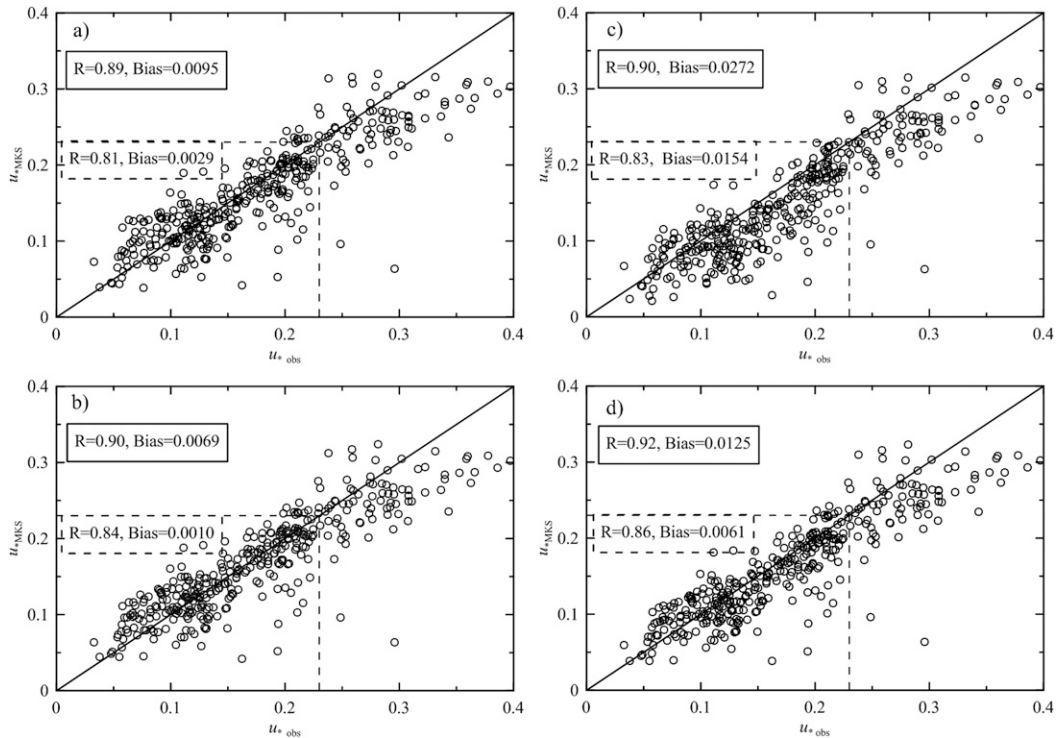


FIG. 5. Comparison between observed and modeled wind stress generated by (a) a wind wave only, (b) a wind wave under nonneutral conditions, (c) wind and swell waves, and (d) all factors. The dashed box shows the dataset for $u_* < 0.23 \text{ m s}^{-1}$ ($U_{10} < \sim 5 \text{ m s}^{-1}$). Here, the MKS's turbulent closure scheme is used.

the buoyancy can reduce (enhance) eddy viscosity under stable (unstable) conditions, which makes the wind profile more (less) steep. Compared with the two methods, Fig. 4 shows that wind profile calculated by MOS was more sensitive to the buoyancy than that calculated by MKS.

4. Comparison with observations

a. Data and data processing

The measurements used in this study were made in the Flux Observation Project in the South China Sea (FOPSCS; Zou et al. 2017). During the project, an eddy-correlation system mounted at 20 m above the sea surface was used to observe the flux of momentum, heat, and water vapor between the ocean and atmosphere, and an acoustic wave and current (AWAC) sensor (Nortek, Rud, Norway) deployed on the seabed was used to record the surface displacement once three hours. Each duration for wave measurement is 2048 s with a sampling frequency of 1 Hz.

The momentum, heat fluxes, and wave data between 12 January 2012 and 8 April 2012 were selected for model comparison. Before the estimation of the fluxes, the raw data were subjected to a strict quality control to guarantee

the accuracy of the result. Then, an averaging time of 30 min was chosen to compute momentum fluxes by the eddy correlation method. In addition, the influence of mesoscale motions was detected by Ogive curves. A detailed description of the measurements, including the platform, instruments, and data quality control, is provided by Zou et al. (2017).

The wave spectra were calculated using the surface displacement recorded by the AWAC. Previous studies (e.g., Makin et al. 1995) showed that wave spectra beyond the folding frequency were primarily responsible for the wind stress. Thus, before verifying the model, we first reconstructed the observed wave spectra by adding an equilibrium and dissipation range to the peak region.

The frequency of the equilibrium range was set to $1.5 < \omega/\omega_p < 2.5$. Many studies (Toba 1973; Resio et al. 2001, 2004; Romero and Melville 2010) have suggested that the equilibrium range has a slope of ω^{-4} . In shallow water, Resio et al. (2001) showed that wave spectra also exhibit strong equilibrium range tendencies:

$$\Phi(k) = \frac{\alpha}{2} u_* g^{-1/2} k^{-5/2}, \quad (23)$$

where k is the wavenumber, which is related to ω by the dispersion relation $\omega^2 = gk \tanh(kh)$. The water depth h

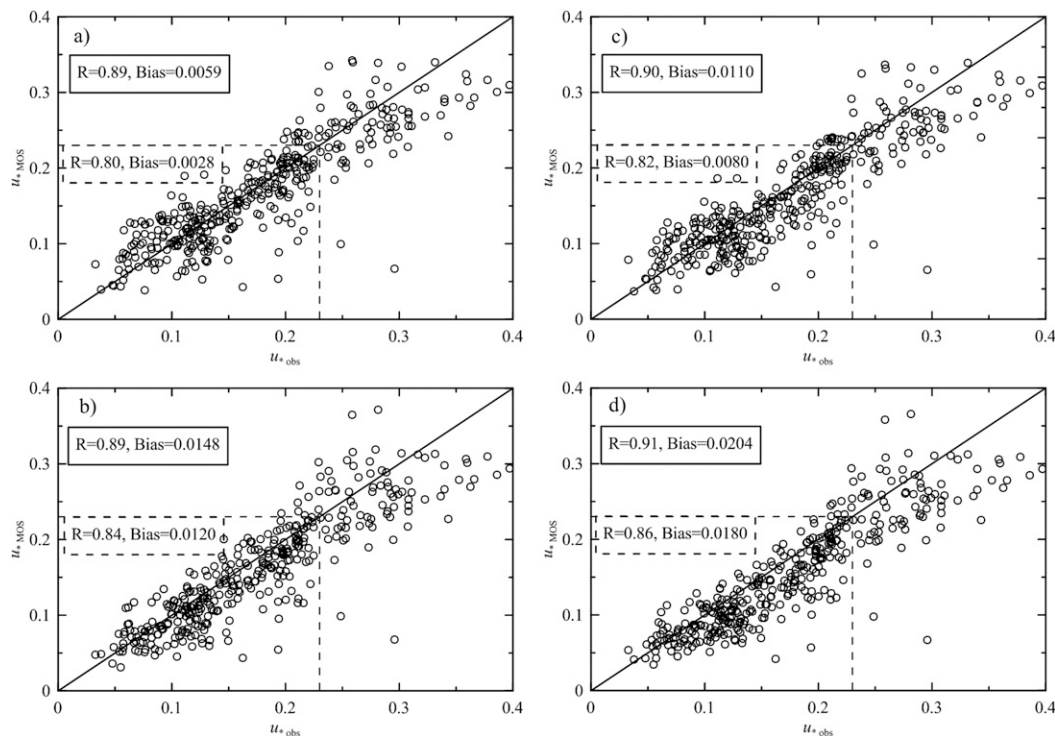


FIG. 6. As in Fig. 5, but for the MOS turbulent closure scheme.

was 14 m in our observations. The α is an empirical parameter and can be expressed as a function of wave age according to [Romero and Melville \(2010\)](#):

$$\alpha = 0.016 \left(\frac{c_p}{u_*} \right)^{0.53}. \quad (24)$$

Recently, [García-Nava et al. \(2012\)](#) reported that the existence of swell can cause a reduction of energy in the equilibrium range. This may be ascribed to the interaction between swell and local wind that leads to a decrease in wind stress. In this study, we neglected this effect to avoid the complex mechanism behind this phenomenon and focused on the influence of swell on the wind stress.

Because the spectra of the dissipation range for ω/ω_p was ≥ 2.5 , a spectral tail proportional to ω^{-5} was imposed. [Long and Resio \(2007\)](#) and [Tamura et al. \(2014\)](#) showed that a transition exists between the equilibrium range and dissipation range, although the explicit form of this transition has not been given until now. Thus, we ignored it and attached the dissipation range directly to the equilibrium range.

b. Results

In this section, the wind stress from the models was compared with measurements from the FOPSCS. The

observed wind speed, Obukhov length scale, and reconstructed wave spectra were input into the model. The wave growth/decay rate coefficient was not clear until now because it depends strongly on the turbulence closure scheme ([Belcher and Hunt 1993](#); [Hanley and Belcher 2008](#)). In this section, a value of 40 was used as the wave growth rate coefficient because it fit the measurement well under wind-wave conditions. For swell conditions, we selected a value of -30 to analyze the effect on wind stress. The sensitivity to this parameter is explored in the next section.

[Figures 5 and 6](#) show comparisons between observed wind stress and the results computed from different turbulent closure schemes. To check if swell and buoyancy have an effect on the wind stress, four cases were considered here: 1) Only wind-wave spectra were input into the model, while the Obukhov length scale was set to ∞ . 2) The wind-wave spectra and observed Obukhov length scale were used to generate wind stress. 3) Both wind-wave and swell spectra under neutral conditions were input into the model. 4) All of the wind-wave and swell wave spectra and the observed Obukhov length were considered.

The results showed a good quantitative agreement between observed and modeled wind stress. After considering the influence of buoyancy and swell (cases 2 and 3 above), both of the correlation coefficients were improved. In the case of a wind wave, our results showed that the influence of buoyancy had a greater impact than swell

in both schemes. However, the model produced the best results by considering all the factors.

The results for the two schemes were generally consistent with each other. However, under non-neutral conditions, the MOS scheme generated a greater bias than the MKS scheme because the mixing length of the former was more influenced by buoyancy.

A careful inspection of the results showed that the wind stress was more affected by buoyancy and swell at low wind speeds when the turbulence generated by shear was weak. Thus, we recomputed the correlation coefficient and bias for $u_* < 0.23 \text{ m s}^{-1}$ ($U_{10} < \sim 5 \text{ m s}^{-1}$). The results are given in the dashed box. It can be seen that the correlation coefficient was significantly improved by considering the effect of swell and buoyancy. The correlation coefficient for MKS increased from 0.81 to 0.86, and for MOS it increased from 0.80 to 0.86.

c. Sensitivity to the swell decay rate

The swell is usually characterized as waves that are generated by distant storms that can propagate for thousands of kilometers, with a small decay rate. During this process, the swell can lose energy to the atmosphere and transfer energy to the oceanic mixed layer (Ardhuin and Jenkins 2006). Although some studies (Babanin and Haus 2009; Ardhuin et al. 2009; Collard et al. 2009; Young et al. 2013) have given various decay rates β based on laboratory and field experiments, synthetic-aperture radar (SAR) images, and altimeter data, they could not separate the quantitative contributions of the atmosphere and ocean and did not directly give the decay rate coefficient c_β .

To investigate the sensitivity of our results to c_β , we set c_β as -10 , -20 , -30 , -40 , -50 , -60 , -80 , or -100 in calculations. All factors, including wind, swell, and buoyancy, are considered in the calculation. Figures 7 and 8 present the results with $c_\beta = -10$, -60 , or -80 for MKS and MOS, respectively. The results show that the influence of c_β was remarkable, especially at low wind speeds. The greater the amplitude of c_β , the greater the bias. This was the same for the other cases. It is clear that this phenomenon accounted for the larger negative swell-induced stress generated by the greater amplitude of decay rate.

Combining Figs. 5 and 6, where $c_\beta = -30$ is used, it was found that MOS was more sensitive to buoyancy than MKS. It is striking that the best results were obtained when $c_\beta = -30$ was used in both MKS and MOS. However, this does not imply that $c_\beta = -30$ reflects the real physical process in the swell condition, because it is a tuning parameter in our model and may be invalid for other turbulent closure models. More observations are needed to obtain the physical decay rate coefficient.

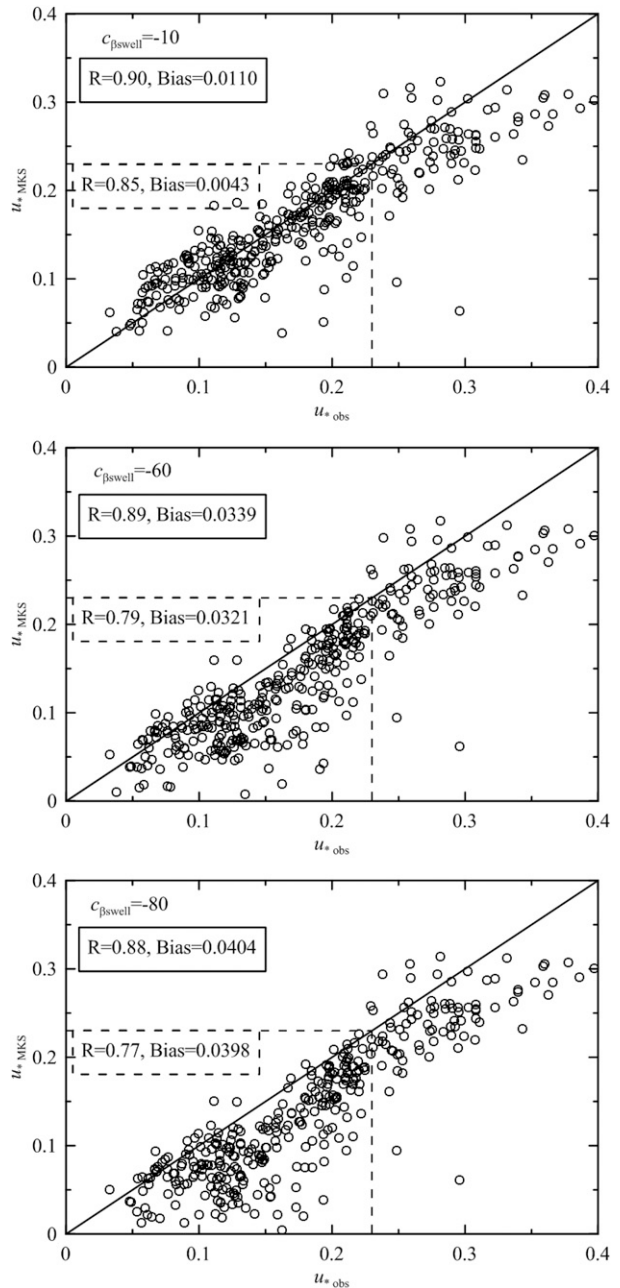


FIG. 7. Sensitivity to the swell wave decay rate for the MKS turbulent closure scheme.

5. Conclusions

This study systematically explored how swell affects the ABL under nonneutral conditions. The constant flux model with two turbulent closure schemes was applied. First, we extended the scheme of Makin and Kudryavtsev (1999) from wind-wave and neutral conditions to swell and nonneutral conditions (MKS). Second, the MOST closure scheme based on wave spectrum (MOS) was applied for comparison.

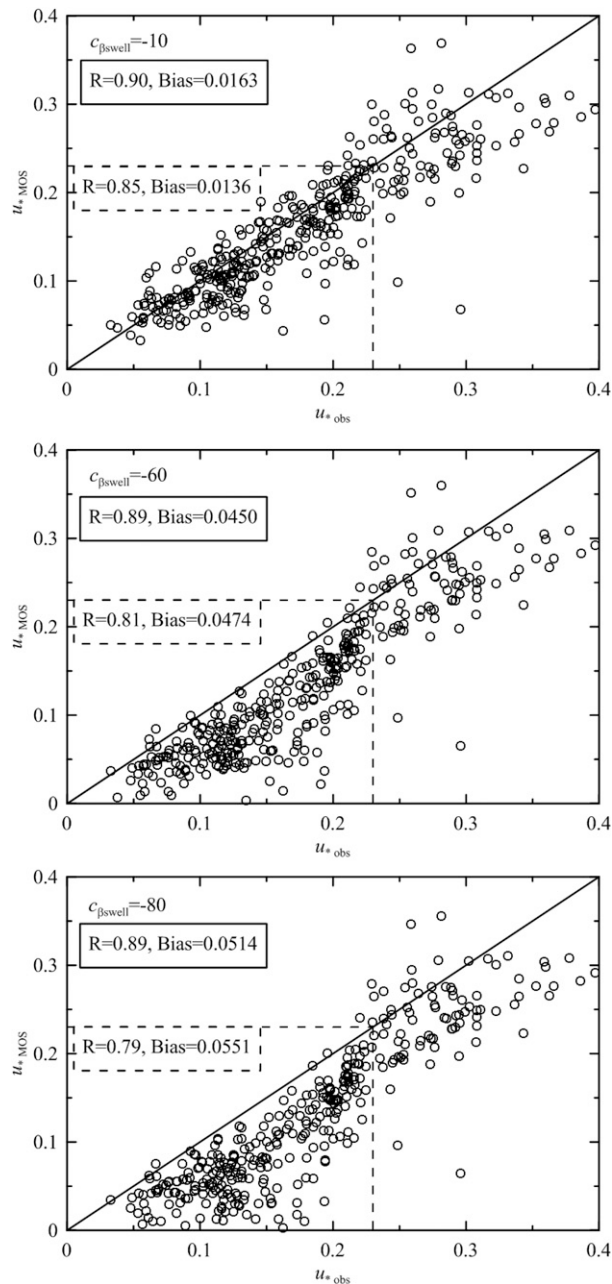


FIG. 8. As in Fig. 7, but for the MOS turbulent closure scheme.

The results show that the influence of swell can penetrate the whole ABL, which would make the traditional MOST invalid. In low wind speed regions, the swell can generate wave-driven jets, a negative gradient mean profile, and negative surface stress. Under nonneutral conditions, buoyancy is another key factor that affects the ABL. In a stable situation, this can lead to an increase in the slope of the wind profile, whereas it makes the wind profile smoother under unstable conditions.

Upon comparison with observations, the importance of the swell and buoyancy for the ABL was confirmed, especially at wind speeds less than 5 m s^{-1} . By considering the effects of a wind wave, swell, and buoyancy, the model can quantitatively capture the behavior of wind stress. Because of the lack of a proper swell decay rate, we investigated the sensitivity of the results to this parameter. It was found that the swell decay rate can significantly alter the bias of the result. Thus, a more physically based swell decay rate is needed for further analysis.

Acknowledgments. We thank the anonymous reviewers for their constructive suggestions that significantly help us improving our manuscript. We gratefully acknowledge the support of the Public Science and Technology Research Funds Projects of Ocean (201505007), the Joint Project for National Oceanographic Center by the National Natural Science Foundation of China (NSFC) and Shandong Government (U1406402), the NSCF (41276015, 41406041, 413776125, 41606024, 41776029), Natural Science Foundation of Guangdong Province (2016A030313751), the Program for Reform and Development of the School of Guangdong Educational Committee (GDOU2016050242), the Special Foundation for Young Teachers of Guangdong Ocean University (HDYQ2015008), the Top-Notch Academic Programs Project of Jiangsu Higher Education Institutions (TAPP), the Fundamental Research Funds for the Central Universities (201762020), and the Priority Academic Program Development of Jiangsu Higher Education Institutions (PAPD).

REFERENCES

- Ardhuin, F., and A. D. Jenkins, 2006: On the interaction of surface waves and upper ocean turbulence. *J. Phys. Oceanogr.*, **36**, 551–557, <https://doi.org/10.1175/JPO2862.1>.
- , B. Chapron, and F. Collard, 2009: Observation of swell dissipation across oceans. *Geophys. Res. Lett.*, **36**, L06607, <https://doi.org/10.1029/2008GL037030>.
- Babain, A. V., and B. K. Haus, 2009: On the existence of water turbulence induced by nonbreaking surface waves. *J. Phys. Oceanogr.*, **39**, 2675–2679, <https://doi.org/10.1175/2009JPO4202.1>.
- Belcher, S. E., and J. C. R. Hunt, 1993: Turbulent shear flow over slowly moving waves. *J. Fluid Mech.*, **251**, 109–148, <https://doi.org/10.1017/S0022112093003350>.
- Charnock, H., 1995: Wind stress on a water surface. *Quart. J. Roy. Meteor. Soc.*, **81**, 639–640, <https://doi.org/10.1002/qj.49708135027>.
- Cohen, J. E., and S. E. Belcher, 1999: Turbulent shear flow over fast-moving waves. *J. Fluid Mech.*, **386**, 345–371, <https://doi.org/10.1017/S0022112099004383>.
- Collard, F., F. Ardhuin, and B. Chapron, 2009: Monitoring and analysis of ocean swell fields from space: New methods for routine observations. *J. Geophys. Res.*, **114**, C07023, <https://doi.org/10.1029/2008JC005215>.
- Donelan, M. A., J. Hamilton, and W. Hui, 1985: Directional spectra of wind-generated waves. *Philos. Trans. Roy. Soc. London*, **A315**, 509–562, <https://doi.org/10.1098/rsta.1985.0054>.

- , W. M. Drennan, and K. B. Katsaros, 1997: The air–sea momentum flux in conditions of wind sea and swell. *J. Phys. Oceanogr.*, **27**, 2087–2099, [https://doi.org/10.1175/1520-0485\(1997\)027<2087:TASMF1>2.0.CO;2](https://doi.org/10.1175/1520-0485(1997)027<2087:TASMF1>2.0.CO;2).
- Drennan, W. M., K. K. Kahma, and M. A. Donelan, 1999: On momentum flux and velocity spectra over waves. *Bound.-Layer Meteor.*, **92**, 489–515, <https://doi.org/10.1023/A:1002054820455>.
- Edson, J., and Coauthors, 2013: On the exchange of momentum over the open ocean. *J. Phys. Oceanogr.*, **43**, 1589–1610, <https://doi.org/10.1175/JPO-D-12-0173.1>.
- Elfouhaily, T., B. Chapron, K. Katsaros, and D. Vandemark, 1997: A unified directional spectrum for long and short wind-driven waves. *J. Geophys. Res.*, **102**, 15 781–15 796, <https://doi.org/10.1029/97JC00467>.
- Fairall, C. W., E. F. Bradley, J. E. Hare, A. A. Grachev, and J. B. Edson, 2003: Bulk parameterization of air–sea fluxes: Updates and verification for the COARE algorithm. *J. Climate*, **16**, 571–591, [https://doi.org/10.1175/1520-0442\(2003\)016<0571:BPOASF>2.0.CO;2](https://doi.org/10.1175/1520-0442(2003)016<0571:BPOASF>2.0.CO;2).
- García-Nava, H., F. J. Ocampo-Torres, P. A. Hwang, and P. Osuna, 2012: Reduction of wind stress due to swell at high wind conditions. *J. Geophys. Res.*, **117**, C00J11, <https://doi.org/10.1029/2011JC007833>.
- Grachev, A. A., and C. W. Fairall, 2001: Upward momentum transfer in the marine boundary layer. *J. Phys. Oceanogr.*, **31**, 1698–1711, [https://doi.org/10.1175/1520-0485\(2001\)031<1698:UMTITM>2.0.CO;2](https://doi.org/10.1175/1520-0485(2001)031<1698:UMTITM>2.0.CO;2).
- Hanley, K. E., and S. E. Belcher, 2008: Wave-driven wind jets in the marine atmospheric boundary layer. *J. Atmos. Sci.*, **65**, 2646–2660, <https://doi.org/10.1175/2007JAS2562.1>.
- Harris, D. L., 1966: The wave-driven wind. *J. Atmos. Sci.*, **23**, 688–693, [https://doi.org/10.1175/1520-0469\(1966\)023<0688:TWDW>2.0.CO;2](https://doi.org/10.1175/1520-0469(1966)023<0688:TWDW>2.0.CO;2).
- Högström, U. L. F., 1988: Non-dimensional wind and temperature profiles in the atmospheric surface layer: A re-evaluation. *Bound.-Layer Meteor.*, **42**, 55–78, <https://doi.org/10.1007/BF00119875>.
- , E. Sahlée, A. S. Smedman, A. Rutgersson, E. Nilsson, K. K. Kahma, and W. M. Drennan, 2015: Surface stress over the ocean in swell-dominated conditions during moderate winds. *J. Atmos. Sci.*, **72**, 4777–4795, <https://doi.org/10.1175/JAS-D-15-0139.1>.
- Jiang, Q., P. Sullivan, S. Wang, J. Doyle, and L. Vincent, 2016: Impact of swell on air–sea momentum flux and marine boundary layer under low-wind conditions. *J. Atmos. Sci.*, **73**, 2683–2697, <https://doi.org/10.1175/JAS-D-15-0200.1>.
- Kihara, N., H. Hanazaki, T. Mizuya, and H. Ueda, 2007: Relationship between airflow at the critical height and momentum transfer to the traveling waves. *Phys. Fluids*, **19**, 015102, <https://doi.org/10.1063/1.2409736>.
- Kudryavtsev, V. N., and V. K. Makin, 2001: The impact of air-flow separation on the drag of the sea surface. *Bound.-Layer Meteor.*, **98**, 155–171, <https://doi.org/10.1023/A:1018719917275>.
- Kundu, P. K., I. M. Cohen, and D. Dowling, 2012: Turbulent energy cascade and spectrum. *Fluid Mechanics*, 5th ed. P. Kundu, I. Cohen, and D. Dowling, Eds., Elsevier Academic Press, 564–566.
- Large, W. G., and S. Pond, 1982: Sensible and latent heat flux measurements over the ocean. *J. Phys. Oceanogr.*, **12**, 464–482, [https://doi.org/10.1175/1520-0485\(1982\)012<0464:SALHFM>2.0.CO;2](https://doi.org/10.1175/1520-0485(1982)012<0464:SALHFM>2.0.CO;2).
- Long, C. E., and D. T. Resio, 2007: Wind wave spectral observations in Currituck Sound, North Carolina. *J. Geophys. Res.*, **112**, C05001, <https://doi.org/10.1029/2006JC003835>.
- Makin, V. K., and V. N. Kudryavtsev, 1999: Coupled sea surface-atmosphere model: 1. Wind over waves coupling. *J. Geophys. Res.*, **104**, 7613–7623, <https://doi.org/10.1029/1999JC900006>.
- , and —, 2002: Impact of dominant waves on sea drag. *Bound.-Layer Meteor.*, **103**, 83–99, <https://doi.org/10.1023/A:1014591222717>.
- , —, and C. Mastenbroek, 1995: Drag of the sea surface. *Bound.-Layer Meteor.*, **73**, 159–182, <https://doi.org/10.1007/BF00708935>.
- Miller, S., C. Friehe, T. Hristov, J. Edson, and S. Wetzel, 1999: Wind and turbulence profiles in the surface layer over ocean waves. *Wind-over-Wave Couplings*, S. Sajjadi, N. Thomas, and J. Hunt, Eds., Institute of Mathematics and Its Applications Conference Series, Vol. 69, Oxford University Press, 91–98.
- Monin, A. S., and A. M. Yaglom, 1971: *Statistical Fluid Mechanics*. Vol. 1. MIT Press, 769 pp.
- Moon, I. J., T. Hara, I. Ginis, S. E. Belcher, and H. L. Tolman, 2004: Effect of surface waves on air–sea momentum exchange. Part I: Effect of mature and growing seas. *J. Atmos. Sci.*, **61**, 2321–2333, [https://doi.org/10.1175/1520-0469\(2004\)061<2321:EOSWOA>2.0.CO;2](https://doi.org/10.1175/1520-0469(2004)061<2321:EOSWOA>2.0.CO;2).
- Mueller, J. A., and F. Veron, 2009: Nonlinear formulation of the bulk surface stress over breaking waves: Feedback mechanisms from air-flow separation. *Bound.-Layer Meteor.*, **130**, 117–134, <https://doi.org/10.1007/s10546-008-9334-6>.
- Nilsson, E. O., A. Rutgersson, A. S. Smedman, and P. P. Sullivan, 2012: Convective boundary-layer structure in the presence of wind-following swell. *Quart. J. Roy. Meteor. Soc.*, **138**, 1476–1489, <https://doi.org/10.1002/qj.1898>.
- Plant, W. J., 1982: A relationship between wind stress and wave slope. *J. Geophys. Res.*, **87**, 1961–1967, <https://doi.org/10.1029/JC087iC03p01961>.
- Reichl, B. G., T. Hara, and I. Ginis, 2014: Sea state dependence of the wind stress over the ocean under hurricane winds. *J. Geophys. Res. Oceans*, **119**, 30–51, <https://doi.org/10.1002/2013JC009289>.
- Resio, D. T., J. H. Pihl, B. A. Tracy, and C. L. Vincent, 2001: Nonlinear energy fluxes and the finite depth equilibrium range in wave spectra. *J. Geophys. Res.*, **106**, 6985–7000, <https://doi.org/10.1029/2000JC900153>.
- , C. E. Long, and C. L. Vincent, 2004: Equilibrium-range constant in wind-generated wave spectra. *J. Geophys. Res.*, **109**, C01018, <https://doi.org/10.1029/2003JC001788>.
- Rieder, K. F., and J. A. Smith, 1998: Removing wave effects from the wind stress vector. *J. Geophys. Res.*, **103**, 1363–1374, <https://doi.org/10.1029/97JC02571>.
- Romero, L., and W. K. Melville, 2010: Airborne observations of fetch-limited waves in the Gulf of Tehuantepec. *J. Phys. Oceanogr.*, **40**, 441–465, <https://doi.org/10.1175/2009JPO4127.1>.
- Rutgersson, A., A. S. Smedman, and U. Högström, 2001: Use of conventional stability parameters during swell. *J. Geophys. Res.*, **106**, 27 117–27 134, <https://doi.org/10.1029/2000JC000543>.
- Semedo, A., Ø. Saetra, A. Rutgersson, K. K. Kahma, and H. Pettersson, 2009: Wave-induced wind in the marine boundary layer. *J. Atmos. Sci.*, **66**, 2256–2271, <https://doi.org/10.1175/2009JAS3018.1>.
- Smedman, A., U. Högström, H. Bergström, A. Rutgersson, K. K. Kahma, and H. Pettersson, 1999: A case study of air–sea interaction during swell conditions. *J. Geophys. Res.*, **104**, 25 833–25 851, <https://doi.org/10.1029/1999JC900213>.
- Song, J., W. Fan, S. Li, and M. Zhou, 2015: Impact of surface waves on the steady near-surface wind profiles over the ocean. *Bound.-Layer Meteor.*, **155**, 111–127, <https://doi.org/10.1007/s10546-014-9983-6>.

- Sullivan, P. P., J. C. McWilliams, and C. H. Moeng, 2000: Simulation of turbulent flow over idealized water waves. *J. Fluid Mech.*, **404**, 47–85, <https://doi.org/10.1017/S0022112099006965>.
- , J. B. Edson, T. Hristov, and J. C. McWilliams, 2008: Large-eddy simulations and observations of atmospheric marine boundary layers above nonequilibrium surface waves. *J. Atmos. Sci.*, **65**, 1225–1245, <https://doi.org/10.1175/2007JAS2427.1>.
- , J. C. McWilliams, and E. G. Patton, 2014: Large-eddy simulation of marine atmospheric boundary layers above a spectrum of moving waves. *J. Atmos. Sci.*, **71**, 4001–4027, <https://doi.org/10.1175/JAS-D-14-0095.1>.
- Tamura, H., W. M. Drennan, E. Sahlée, and H. C. Graber, 2014: Spectral form and source term balance of short gravity wind waves. *J. Geophys. Res. Oceans*, **119**, 7406–7419, <https://doi.org/10.1002/2014JC009869>.
- Toba, Y., 1973: Local balance in the air-sea boundary processes. *J. Oceanogr. Soc. Japan*, **29**, 209–220, <https://doi.org/10.1007/BF02108528>.
- Young, I. R., A. V. Babanin, and S. Zieger, 2013: The decay rate of ocean swell observed by altimeter. *J. Phys. Oceanogr.*, **43**, 2322–2333, <https://doi.org/10.1175/JPO-D-13-083.1>.
- Zou, Z., D. Zhao, B. Liu, J. A. Zhang, and J. Huang, 2017: Observation-based parameterization of air-sea fluxes in terms of wind speed and atmospheric stability under low-to-moderate wind conditions. *J. Geophys. Res. Oceans*, **122**, 4123–4142, <https://doi.org/10.1002/2016JC012399>.